Evaluation of 3D printed monolithic G-band waveguide components

Skaik, Talal; Salek, Milan; Hunyor, Peter; Wang, Hui; Huggard, Peter G.; Wilson, Paul F.; Williams, Mark A.; Wang, Yi

DOI:
10.1109/TCPMT.2023.3243002

Evaluation of 3D Printed Monolithic G-band Waveguide Components

Talal Skaik, Milan Salek, Peter Hunyor, Hui Wang, Peter G. Huggard, Paul F. Wilson, Mark A. Williams and Yi Wang

***Abstract*— This paper presents a comprehensive evaluation of 3D-printed monolithic waveguide components fabricated by a high-precision micro laser sintering (MLS) process. The investigated devices are two 180 GHz bandpass filters and a straight G-band (140-220 GHz) waveguide section. All were made of stainless steel, which was later gold coated using an electroless process. One of the filter samples was characterized using X-ray micro-CT to inspect the printing quality as well as measure the internal dimensions. The sample was then sectioned to allow measurement of the surface roughness of the inner surfaces and inspect the gold coating quality. The as-manufactured stainless steel components showed high insertion losses: over 3 dB in the filter passbands and between 4.7 dB and 7 dB for the waveguide section, increasing with frequency over the G-band. This loss is due to the electrical conductivity of stainless steel as well as the surface roughness. Gold plating significantly reduced the insertion losses, to 0.5 dB for the filters and to between 0.6 dB and 1 dB for the waveguide section. The investigative study showed the high dimensional accuracy and good printing quality achieved by MLS, demonstrating the value of the technique in producing monolithic metal waveguide components with fine geometrics.**

***Index Terms*—3D printing, G-band, micro laser sintering (MLS), waveguide filter.**

I. Introduction

3D-PRINTING technology has been extensively investigated as a new fabrication route for microwave components based on waveguide structures. A number of processes are currently available, including fused deposition modeling (FDM) [1], stereolithography apparatus (SLA) [2] and selective laser sintering (SLS) [3]. The FDM method has inferior accuracy, is suitable for low-cost prototyping and may not be an appropriate solution for millimeter-wave devices. The SLA process is polymer-based, provides the highest dimensional accuracy among the three methods, and components exhibit excellent surface finish. However, metal plating is required. The SLS is a metal-based technique and a strong contender for mm-wave components owing to accuracy as well as good mechanical and thermal properties. SLS is also known as selective laser melting (SLM) or micro laser sintering (MLS) that produces micro metal parts. However, surface roughness of the as-printed metallic parts remains a problem for devices that require low insertion losses. Moreover, SLS process with relatively low conductivity metals (e.g. stainless steel) also requires metal plating.

Application of these techniques has been reported for a number of straight rectangular waveguide sections. Metal-coated polymer-based waveguide components were studied at various frequency bands: WR-10 (75-110 GHz) [4], WR-5 (140-220 GHz) [5], WR-3 (220-330 GHz) [6] and WR-1 (750-1100 GHz) [7]. The latter two works exploited the unique capability of 3D printing technology of producing monolithic components, unlike the conventional split-block approach that requires assembly and fasteners. All-metal 3D printed rectangular waveguides have also been reported [8]-[10]. In [8], various monolithic waveguides produced by Cu-15Sn powder using SLM were reported: WR-12 (60-90 GHz), WR-6 (110-170 GHz) and WR-3. In [9], an WR-10 waveguide section manufactured by SLM process was presented. A WR-5 waveguide produced by MLS process was presented in [10]. The performance of these waveguide sections will be compared later in this paper.

Other 3D printed components with more complex structures such as horn antennas [11]-[13] and waveguide filters [13]-[23] were also investigated. Waveguide filters are more challenging, particularly for frequencies above 100 GHz, due to the fine geometries of the coupling irises with wall thicknesses of the order of 100 µm. In [14], an X-band (8.2-12.4 GHz) SLA filter demonstrated the 3D-printing capability in constructing complex spherical resonators. SLA-fabricated filters with rectangular cavity resonators operating from 75-110 GHz were reported in [4] and [15]. Polymer-based 3D-printed G-band filters made of H-plane split blocks were reported in [13], [16]. Those filters required metal plating as an extra step after printing. A number of all-metal filters were also presented in the open literature [17]-[23]. In [17], Ku/K band lowpass filters made by SLM were presented. Reference [18] reports on a Ku-band bandpass filter with ellipsoid cavities fabricated by SLM process. A K-band filter made by aluminum alloy [19]

Manuscript received May 19, 2022. This work is supported by the UK Engineering and Physical Science Research Council under grant EP/S013113/1, EP/P020615/1, EP/T02593X/1 and the Research England funded TALENT programme.

T. Skaik, M. Salek and Y. Wang are with the School of Electrical, Electronic and Systems Engineering, University of Birmingham, Birmingham B15 2TT, U.K. (e-mail: t.f.skaik@bham.ac.uk, m.salek@bham.ac.uk, y.wang.1@bham.ac.uk).

P. Hunyor, H. Wang and P. G. Huggard and are with the STFC Rutherford Appleton Laboratory, RAL Space, Didcot, OX11 0QX, U.K. (e-mail: peter.hunyor@stfc.ac.uk, hui.wang@stfc.ac.uk, peter.huggard@stfc.ac.uk).

P. F. Wilson and Mark A. Williams are with the Centre for Imaging, Metrology, and Additive Technologies (CiMAT) at WMG, University of Warwick, Coventry, CV4 7AL, U.K. (e-mail: Paul.Wilson@warwick.ac.uk, m.a.williams.1@warwick.ac.uk).

and an WR-12 (60-90 GHz) diplexer made by copper-based alloy [20] were also fabricated by SLM technique. In [21], W-band stainless steel filter made by MLS was reported. The authors of this paper previously presented two filters above 100 GHz fabricated by MLS. The first is a G-band (140-220 GHz) filter operating at 180 GHz [22] and the second is an H-band (220-330 GHz) filter operating at 300 GHz [23]. The 180 GHz filter was printed as a monolithic enclosed structure while the 300 GHz filter was made of a split-block of two identical pieces. A literature survey has shown no other reports on 3D-printed filters operating above 100 GHz. This may be attributed to the stringent requirement of high-resolution and high-accuracy (within ±10 µm) printers which are uncommon and expensive. There are also significant challenges associated with the post-processing of such high frequency waveguide filters, especially for those with a monolithic structure. In this context, here we extend the work on the 180 GHz stainless steel filters. In particular, the components were coated with gold using an electroless plating process. Internal structures were investigated using micro X-ray Computed Tomography (XCT). The sample was then sectioned using electrical discharge machining (EDM) to allow further characterization on the surface roughness of the inner surfaces, the internal dimensions and the gold coating quality. The measured mm-wave performance of the gold-coated 3D-printed samples is compared below with that of G-band filters manufactured by other technologies [24]-[28]. Additionally, the loss of a straight G-band waveguide section made by MLS was evaluated to extract the effective electrical conductivity. The performance of this 3D printed section is also benchmarked against commercially available waveguides.

The paper is organized as follows. Section II presents the design method, fabrication technique, gold-plating process and measurement results of the 180 GHz waveguide filter. Section III shows surface characterization and dimensional measurements. Section IV presents the G-band waveguide section and Section V draws conclusions of this work.

II. 180 GHz Waveguide Cavity Filter

A. Filter Design

The filter is designed at 180 GHz, with 11% fractional bandwidth and 20 dB specified return loss. It is formed of inductively coupled waveguide cavity resonators arranged in an inline topology to produce a fifth-order Chebyshev filtering response. The internal air-model of the filter is shown in Fig. 1(a). The filter performance was simulated using CST Microwave Studio [29]. Following a standard filter design technique [30], the dimensions of the coupling irises are adjusted to realize the required inter-resonator coupling coefficients $M_{12} = M_{45} = 0.0961$, $M_{23} = M_{34} = 0.0706$ and the external quality factors $Q_{e1} = Q_{eN} = 8.76$. A top view of the filter is also shown in Fig. 1(a) and the final optimized dimensions are also given. A cross-sectional view and the final physical model of the filter including standard UG387/U waveguide flanges are shown in Fig. 1(b) and Fig. 1(c), respectively. The flanges incorporate air cavities to reduce mass and, more importantly, to alleviate thermal stress induced by the rapid heating and cooling of the MLS process. The hollow structure is a uniquely possible feature of 3D printing. The octagonal perimeter of the flanges, Fig. 1, circumvents the use of supporting structures and the pentagonal shape of the holes in the flanges renders self-support during printing.

B. Filter Fabrication and Plating

Two monolithic filter samples were fabricated in 316L stainless steel using MLS by 3D Microprint GmbH [31]: Fig. 2(a). The printer utilized a laser beam with an average power of 50 W and spot-size of 30 µm to selectively melt and fuse metal powder in successive ≈ 7 µm thick layers. Fine powder was used with a particle size of $D_{90} < 5$ µm. The printing time was about 10 hours. The filter was printed such that central line along the filter is parallel to the building platform and the filter is tilted by 45^0 as shown in Fig. 5 (c). The as-printed parts were blasted with corundum and the planar surfaces of the flanges were mechanically polished. This was done on a sample grinding machine using SiC grinding plates and a basic clamp mount.

An electroless gold plating process was developed to improve the surface conductivity of the stainless steel samples. An initial oxide layer removal was followed by an electroless nickel undercoat, the latter deposited to increase adherence of the subsequentially plated gold. The plating recipe is outlined as follows: (1) rinse, (2) degreasing soak, (3) rinse, (4) acid dip, (5) rinse, (6) Wood's nickel strike, (7) electro-less nickel and (8) immersion/autocatalytic gold plating. A peristaltic pump was used to move the plating solutions along the length of the waveguides. After the part is nickel plated, gold plating is applied in a two-step process. Initially the part is plated with immersion gold (for few minutes only) which only reaches a few nm thick. This is followed by the autocatalytic gold. This

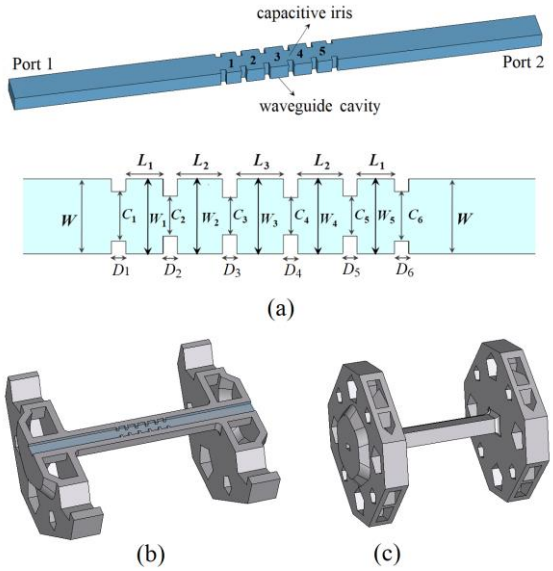

Fig. 1. 180 GHz waveguide filter structure: (a) Air cavity model of the filter and top view with the dimensional parameters; (b) H-plane cross-sectional view showing internal filter structure; (c) Complete design model with hollowed flanges. The dimensions in mm are: $W = W_1 = W_2 = W_3 = W_4 = W_5 = 1.295$, $L_1 = 0.648$, $L_2 = 0.782$, $L_3 = 0.810$, $C_1 = C_6 = 0.857$, $C_2 = C_5 = 0.688$, $C_3 = C_4 = 0.645$ and $D_1 = D_2 = D_3 = D_4 = D_5 = D_6 = 0.250$.

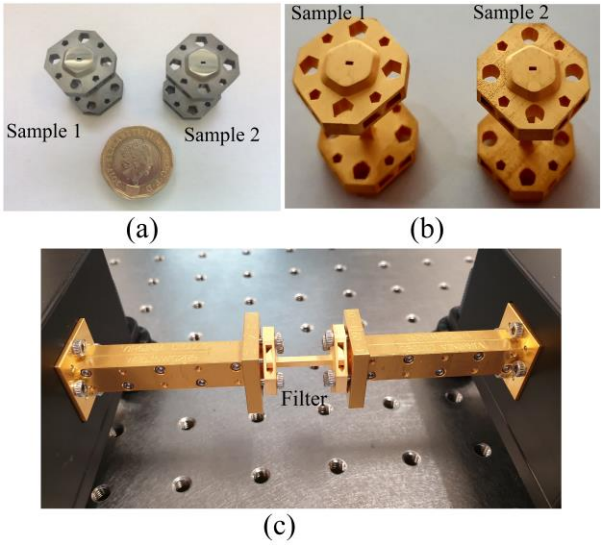

Fig. 2. Photographs of the prototypes: (a) as-printed stainless steel samples; (b) gold-coated samples and (c) measurement setup of the filter.

requires a long time (approximately 6-8 hours) as the plating rate is slow (about 0.4-0.5 µm/hour in ideal conditions) and it is especially slow due to the internal structure of the filter with irises. Temperature control is very important and hence the solution temperature is checked every 30 minutes to make sure it is in range. It should be noted that each filter had been plated a few times.

The electroless nickel and gold plating procedure adopted does not require an anode, cathode, or application DC current like other polishing/plating methods. It is challenging to achieve good gold coverage and uniform thickness due to the internal walls between cavities. These structures impede the flow of the solutions, which may result in insufficient removal of gas bubbles generated during nickel plating (leaving exposed steel areas) and cause turbulent flow, inhibiting the plating rate of the autocatalytic gold. It is expected that the thinnest Ni/Au coverage is at the corners of the filter cavities due to turbulent flow. The solution flow was continuous, and the flow rate was the slowest the pump could do. A reverse flow was also introduced to improve the consistency in plating.

Therefore, five applications of gold were used to ensure good coverage. We targeted a coating thickness of ten times the skin depth, δ = 0.18 µm at 180 GHz, in exposed areas to ensure sufficient coverage over the less accessible areas. A picture of the gold-plated samples is shown in Fig. 2(b). Nickel undercoat was applied before the first and last gold layers. The radio frequency performance of the stainless steel component was measured with the characterization repeated after the application each gold layer.

C. Filter Measurement

A Keysight N5247B PNA-X network analyzer and VDI frequency extension heads were utilized to test the filter samples. A TRL (Thru, Reflect, Line) calibration method was performed first, and the measurement setup is shown in Fig. 2 (c). The calibration moved the reference planes to the ends of the frequency extender waveguides. The measured S-parameters, as well as the simulated results, are given in Fig. 3 for Filter 1 and in Fig. 4 for Filter 2. Results after application of layers of gold are denoted as Gold1, Gold2…, Gold5. Measured results on the stainless steel devices indicate a response curve downshifted by 2.75 GHz for Filter 1 and 2.45 GHz for Filter 2. This can be attributed to fabrication inaccuracies in filter dimensions. Minimum measured insertion loss is 3.0 dB for Filter 1 and 2.9 dB for Filter 2 while the simulated value is 1.8 dB, evaluated using an electrical conductivity of 1.35×10^6 S/m. Measured S_{11} is below -18.3 dB for Filter 1 and below -17.2 dB for Filter 2. Further analysis on larger than simulated insertion losses will be presented in Section III. The first gold plating significantly reduced insertion losses to a minimum of 1.4 dB (Fig. 3 (b)) in Filter 1 and to 2 dB in Filter 2 (Fig. 4(b)). Further improvement is noticeable from the supplemental gold coatings with achieved minimum insertion loss of 0.5 dB in Filter 1 and 0.6 dB in Filter 2 after the final gold coating, Gold 5. However, applying multiple coatings degraded S_{11} to below -14 dB for Filter 1 and to below -13 dB for Filter 2, as measured after final plating.

A noticeable frequency shift upwards is also noticed after the first and last gold plating owing to applying nickel undercoat prior to these coatings. It should be noted that the final nickel undercoat was applied to achieve better adhesion and to add an extra thickness that would cause an upward frequency shift toward the design response. The overall thickness of nickel combined with the gold coating resulted in smaller cavity sizes which caused a noticeable frequency shift.

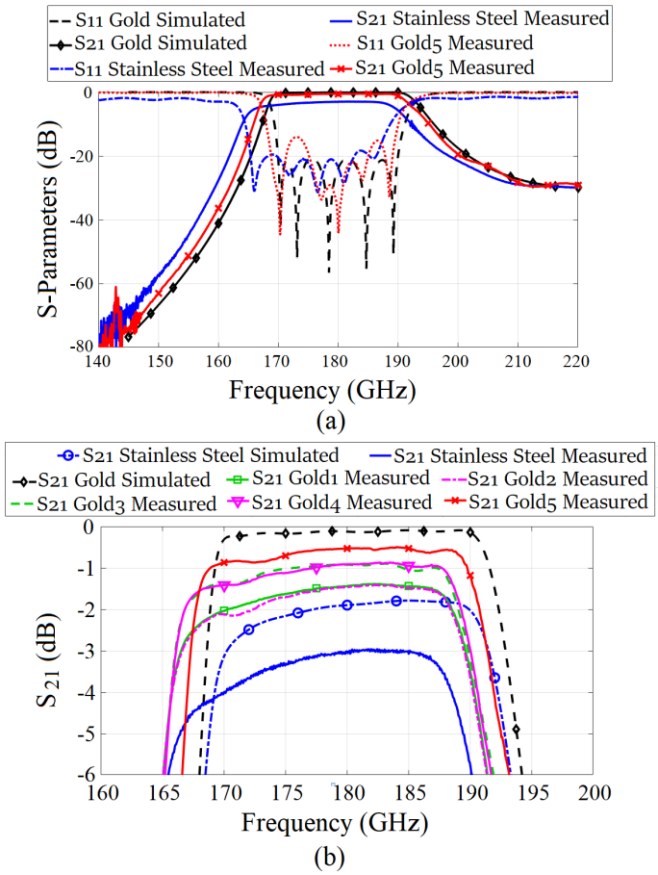

Fig. 3. Simulated and measured results of the Filter 1: (a) S_{11} and S_{21} of the stainless steel device and after five layers of gold, Gold5; (b) Enlarged view of S_{21} of the stainless steel and gold-coated device, showing responses after each stage of gold coating.

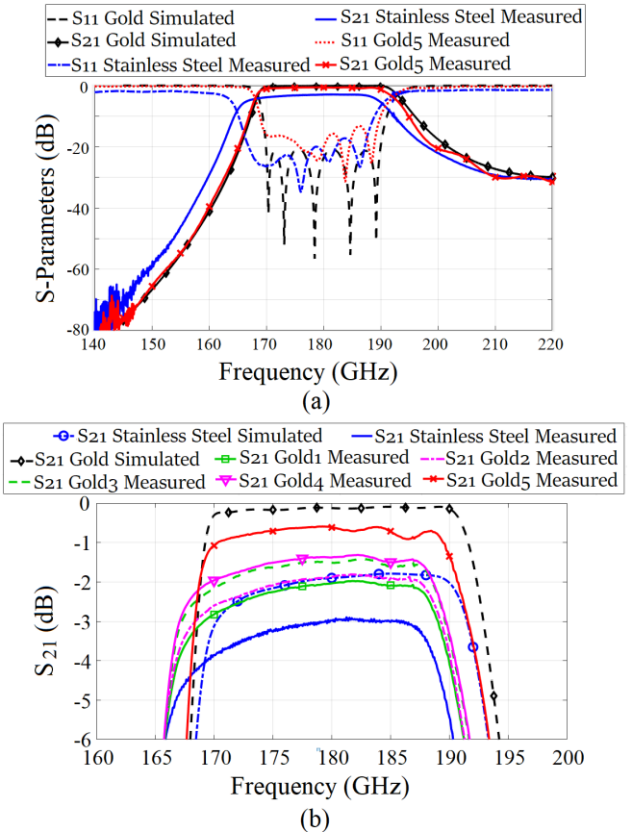

Fig. 4. Simulated and measured results of the Filter 2: (a) S_{11} and S_{21} of the stainless steel device and after five layers of gold, Gold5; (b) Enlarged view of S_{21} of the stainless steel and gold-coated device, showing responses after each stage of gold coating.

The plating thickness may be estimated from simulations based on the frequency shift in center frequencies obtained from the measurements after the coatings. To do so, a simplified simulation model is used. The internal dimensions of the filter are reduced uniformly to account for the effect of plating. The change of the frequency as a function of the coating thickness is established from a series of simulations. According to the measured results of Filter 1, the frequency shift after 1st gold coating (compared to stainless results) is about 0.855 GHz. Based on the simulated relationship between frequency and coating thickness, this corresponds to a coating thickness of around 2 µm. In the subsequent 2nd, 3rd and 4th coatings, only electroless gold plating was applied without Ni undercoating. In 3rd coating, a frequency shift of about 0.39 GHz (compared to 2nd coating response) was observed which corresponds to a gold coating thickness of less than 1 µm. Moreover, improvement in insertion loss of about 0. 54 dB was observed. The 2nd and 4th coatings showed neither frequency shift nor insertion loss improvement indicating ineffective plating. The 5th coating with Ni/Au resulted in a frequency shift of about 1.44 GHz (compared to the 4th coating) which corresponds to a coating thickness of about 3 µm. These estimations from the simulations agree reasonably well with the X-ray fluorescence (XRF) measurements in Fig. 7 that show Ni and Au thickness for the last coating.

The performance of the 3D-printed samples is compared in Table I with other G-band filters made by different technologies such as deep reactive-ion etching (DRIE) [25]-[26], substrate integrated waveguide (SIW) [27] and computer numerical control (CNC) milling [24],[28]. The advantage of the MLS devices over other filters is a monolithic structure. Moreover, the filters exhibit insertion losses comparable with the best alternative techniques. This suggests that the MLS 3D-printing technology can be a strong candidate as a fabrication process for waveguide components operating in the G-band and sub-THz frequencies.

III. Surface Characterization and Dimension Measurements

A high-resolution X-ray micro-CT scanner Zeiss Versa 520S was utilized to measure the internal dimensions and to characterize any porosity of Filter 1. The filter was scanned in three separate sections and later merged to achieve sufficient resolution for accurate visualization, at the following settings: 140kV, 8W, 6s Exposure, HE3 Filter, at 1601 Projections at a voxel resolution of 1.75µm. Voxel scaling was performed with a calibrated artifact to increase spatial accuracy in VGStudio Max 2.2, with plane-to-plane measurements being performed in the same software. Fig. 5(a) shows an image marked with dimensions of the widths of the cavities, also given in Table II. The table also shows the measured lengths of cavities, the widths of irises and thickness of walls and the dimensional parameters *W*, *L*, *C* and *D*, as in Fig. 1.

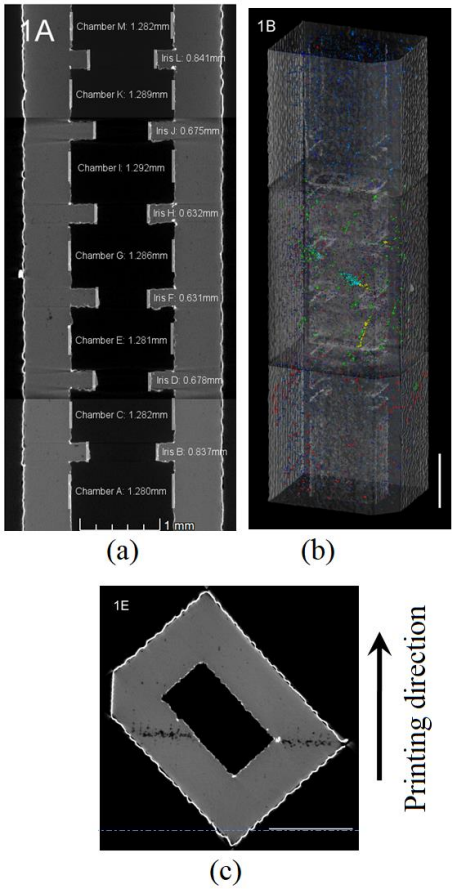

Fig. 5. Micro-CT images of Filter 1: (a) dimension measurements; (b) distribution of pores; (c) cross section at cavity 3. Colors represent pore size as follows: Light Blue = $<10^{-6}$ mm^3, Dark Blue = 10^{-6} mm^3 to $<10^{-5}$ mm^3, Red = 10^{-5} mm^3 to $<10^{-4}$ mm^3, Green = 10^{-4} mm^3 to $<10^{-3}$ mm^3, Yellow = 10^{-3} mm^3 to $<10^{-2}$ mm^3, Turquoise = $>10^{-2}$ mm^3.

TABLE I
COMPARISON WITH OTHER FILTERS

Ref.	Centre Frequency (GHz)	Bandwidth (%)	Filter Order	Minimum Insertion Loss (dB)	Return Loss (dB)	Manufacturing technique	Response
16	181.7	9.3	5	0.6	>13	MSLA*	Chebyshev
24	214.3	9.8 (3dB)	4	0.6	>15	CNC* milling	Quasi-elliptic
25	141.9	10.2	6	0.5	>18	DRIE*	Chebyshev
26	174	5.5	6	1.5	>15	DRIE*	Chebyshev
27	180	8	4	3.2	>15	SIW*	Chebyshev
28	187	2.1	5	1.5	>10	CNC milling	Chebyshev
	217	2.7	5	1.5	>10	CNC milling	Chebyshev
This work Filter 1(2)	180	11	5	0.5 (0.6)	>14 (13)	MLS	Chebyshev

* MSLA: Masked stereolithography apparatus, DRIE: Deep reactive-ion etching, SIW: Substrate integrated waveguide, CNC: Computer numerical control

TABLE II
DESIGN AND MEASURED DIMENSIONS OF FILTER 1

Parameter	Design (µm)	Measured Alicona/µCT (µm)	Mean difference from design (µm)	Parameter	Design (µm)	Measured Alicona/µCT (µm)	Mean difference from design (µm)
L1	648	657/655	+8	C2	688	681/675	-10
L2	782	790/792	+9	C3	645	639/632	-10
L3	810	808/820	+4	C4	645	632/631	-14
L4	782	785 /787	+4	C5	688	686/678	-6
L5	648	654/670	+14	C6	857	841/837	-18
W1	1295	1291/1289	-5	D1	250	224/241	-18
W2	1295	1297/1292	-1	D2	250	221/246	-17
W3	1295	1284/1286	-10	D3	250	238/253	-5
W4	1295	1281/1281	-14	D4	250	240/248	-6
W5	1295	1286/1282	-11	D5	250	236/243	-11
C1	857	849/841	-12	D6	250	236/243	-11

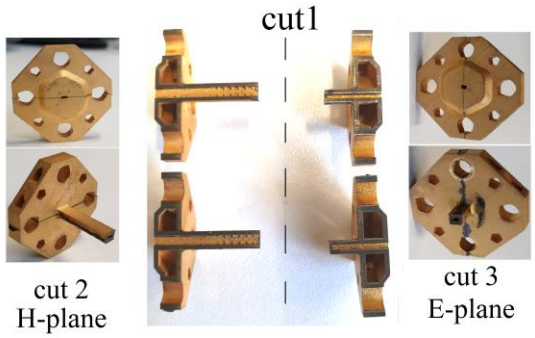

Fig. 6. Photographs of filter 1 after cutting along E-plane and H-plane.

The table also includes dimensions measured by Alicona G4 InfiniteFocus optical microscope [32] after the filter was sectioned, as explained later. Table II presents the average deviations of the measured dimensions from the design values: it is found that dimensional accuracy is within ±10 µm. The measured lengths of the cavities, L_1 to L_5, are larger than the design values. This may be partly due to the reduced thickness of the iris walls, denoted by D_1 to D_6. The widths of cavities W_1 to W_5, as well as coupling aperture sizes C_1 to C_6, are also smaller than the design.

Fig. 5(b) shows distribution of pores across the sample. It is noticed that pores are generally scattered evenly across the sample except for a noticeable line defect running diagonally through the filter around cavity 3, as shown in Fig. 5(c). There is no concentration of pores around the internal surfaces, so they should have a relatively insignificant impact on the RF performance. The study reported in [33] investigated the electrical conductivity and porosity in stainless steel 316L scaffolds fabricated using selective laser sintering process. The findings show existence of pores in the printed samples with apparent decrease in electrical conductivity from about 3.2×10^6 S/m to 1×10^6 S/m, with the increase of bulk porosity from 4% to 22%.

To investigate the internal surfaces of the enclosed filter and to directly measure the filter dimensions, Filter 1 was cut into several pieces using electric discharge machining (EDM), as shown in Fig. 6. The first cut, "cut1", is across the waveguide and separated the waveguide cavities from the feed. The second cut, "cut 2", was applied along the H-plane to the part containing the cavities. It allowed access to the top and bottom surfaces of the cavities/waveguides. The part with the feed was sliced along the E-plane, "cut 3". It allowed access to the side walls of the feeding waveguide. The internal dimensions of the filter were measured using the Alicona optical microscope, and compared to the design values in Table II, as mentioned earlier. The thickness of the nickel and gold plating was measured for both the E/H-plane-cut parts using X-ray fluorescence (XRF) analyzer. Results are shown in Fig. 7. It should be noted that the measured values represent the final gold coating over nickel undercoat. Various areas were measured, and the results show a gold thickness varying between 0.6 µm and 1.73 µm.

The range of thicknesses is attributed to the flow of the plating solution that is different around the edges of the sample from other locations. The thickness of the nickel undercoat is also variable, at between 1.53 µm and 2.32 µm. The surface roughness of the internal surfaces was characterized utilizing the optical microscope. Fig. 8 shows photographs for the bases, i.e. broad walls, of the waveguide cavities and the surface roughness S_a measured over a selected area of about 0.7 mm × 0.7 mm. The average value of S_a at the bases of the five cavities is 3.8 µm. The surface roughness of the waveguide sidewall in the E-plane block was also characterized: Fig. 9. The average S_a at two measured locations is about 3.45 µm. Considering S_a=3.65 µm as an average roughness of both the bases and the

sidewalls, the effective electrical conductivity of stainless steel would degrade to about 3.5×10^5 S/m using Hammerstad-Jensen model [34]. Similarly, gold electrical conductivity is reduced to an effective value of 1.1×10^7 S/m. The filter performance was simulated with the modified conductivity. As shown in Fig. 10, the simulation results agree much better with the simulation when an ideal gold conductivity was used. This validates the explanation that surface roughness is a dominant factor causing the additional insertion losses. Moreover, the similarity in performance between the two gold-plated filters indicates excellent printing repeatability as well as gold coating consistency.

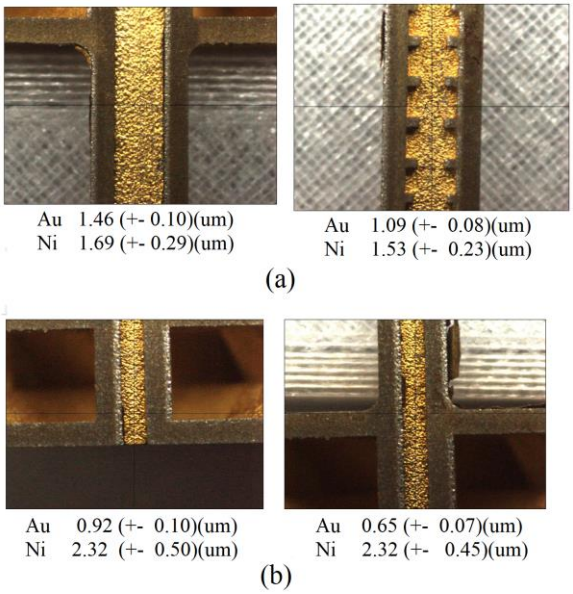

Fig. 7. XRF images of Filter 1 after EDM cut for gold and nickel thickness measurement (a) H-plane-cut part and (b) E-plane-cut part.

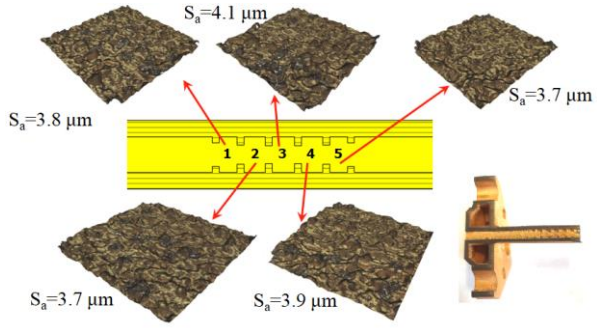

Fig. 8. Surface roughness characterization of the H-plane block at the bases of the waveguide cavities.

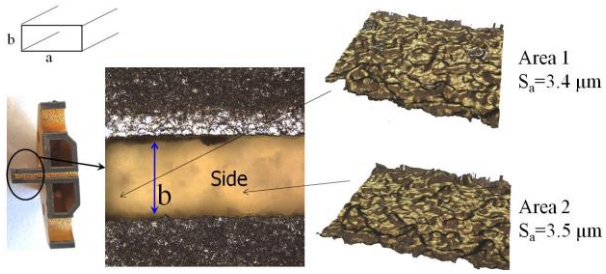

Fig. 9. Surface roughness characterization of the E-plane block at the sidewalls of the waveguide.

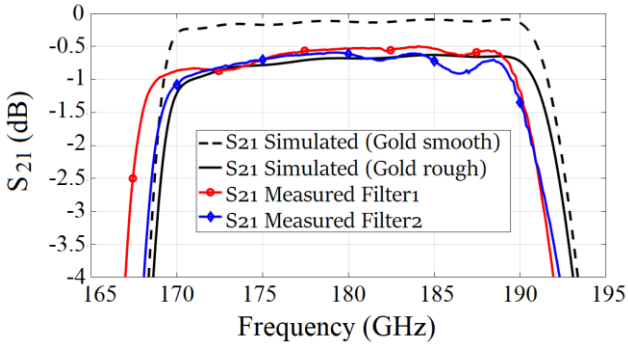

Fig. 10. Simulated S_{21} using the effective gold conductivity due to surface roughness, compared to measured results of both filters.

IV. G-band Waveguide Section

A straight G-band waveguide section was also fabricated using MLS to characterize independently the losses and extract the effective conductivities of the stainless steel and the gold. This was a 50.8 mm (2 inch) long section that was built as one monolithic block of stainless steel and gold-plated twice. Pictures of the fabricated waveguide section before and after gold plating are shown in Fig. 11. Similar hollowed octagonal-shape flanges as in the filters are used. The S-parameters of the 3D-printed waveguide were measured and compared with those of a standard section from Virginia Diodes Inc. (VDI) with the same length, shown in Fig. 11 (a). Simulated and measured results of both waveguide sections are shown in Fig. 12(a). The stainless steel waveguide shows a reflection coefficient, S_{11}, of below -20 dB, worse than that of the VDI section, measured below -30 dB. Gold plating degraded the S_{11} of the printed waveguide to an average better than -20 dB and a worst case ≈ -16 dB. An enlarged view of S_{21} data is shown in Fig. 12(b). S_{21} for the stainless steel section increases with frequency from -7 dB to -4.7 dB over the G-band. The simulated S_{21} is between -3.5 dB and -2.2 dB, estimated from a nominal electrical conductivity of 1.35×10^6 S/m. Assuming a surface roughness of S_a=3.65 µm, taken from the measured value of the 180 GHz filter, the effective conductivity degrades to 3.5×10^5 S/m. The simulated S_{21} ranges between -6.8 dB to -4.4 dB, in very good agreement with the measurement, indicating the surface roughness is the main contributor to the excess insertion losses.

The first gold plating of the 3D printed waveguide significantly improved S_{21} to between -1.6 dB and -0.85 dB, while the second coating further enhanced S_{21} to be between -1 dB and -0.7 dB. Simulation results with ideal gold conductivity of 4.4×10^7 S/m show S_{21} between -0.6 dB and -0.4 dB.

TABLE III
Insertion Loss of 2 inch Long Waveguide Section at 180 GHz

	IL (dB)
Simulated stainless steel – smooth (σ=1.35×10^6 S/m)	2.45
Simulated stainless steel – rough, S_a=3.6 µm (σ_{eff}=3.5×10^5 S/m)	4.80
Measured stainless steel	4.95
Simulated gold – smooth (σ=4.4×10^7 S/m)	0.43
Simulated gold – rough, S_a=3.6 µm (σ_{eff}=1.1×10^7 S/m)	0.85
Measured gold1	0.85
Measured gold2	0.80
Measured standard VDI	0.39

TABLE IV
COMPARISON OF WAVEGUIDE LOSSES AS FUNCTIONS OF FREQUENCY AND MANUFACTURING APPROACH

Ref.	Waveguide	Frequency range (GHz)	Technology	Material	Monolithic/ split-block	Attenuation (dB/m)
4	WR-10	75-110	SLA	Plated polymer	Split	11 at 110 GHz
5	WR-5	140-220	Polyjet 3D printing	Plated polymer	Split	59 at 172 GHz
6	WR-3	220-330	SLA	Plated polymer	Monolithic	~13 at 280 GHz*
7	WR-1	750-1100	3D printing	Plated polymer	Monolithic	1425 at 925 GHz
8	WR-12	60-90				7.76 (average)
	WR-6	110-170	SLM	Copper alloy	Monolithic	21.47 (average)
	WR-3	220-330				93.82 (average)
9	WR-10	75-110	SLM	Ti-6Al-4V alloy	Monolithic	30.4 at 94 GHz
10	WR-5	140-220	MLS	Stainless steel	Monolithic	90 at 220 GHz
Standard VDI	WR-5	140-220	NA	NA	Split	7.7 at 180 GHz*
This work	WR-5	140-220	MLS	Stainless steel / Gold-coated	Monolithic	98 at 180 GHz*/ 15 at 180 GHz*

* Dissipative attenuation is calculated using equation (1).

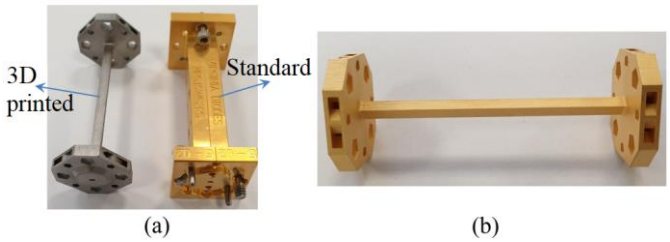

Fig. 11. Photographs of the 2-inch waveguide sections: (a) 3D printed waveguide section (left) standard section from VDI (right) and (b) gold-coated 3D printed waveguide section.

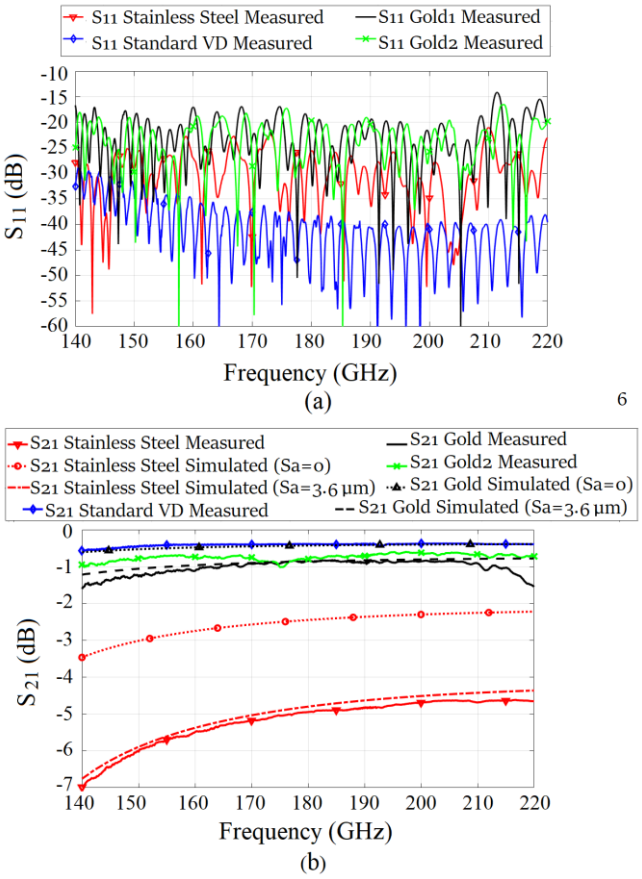

Fig. 12. Simulated and measured results of the 3D printed and standard VDI waveguide sections: (a) S_{11} and S_{21}; (b) Enlarged view of S_{21}.

Again, due to surface roughness, the effective electrical conductivity of gold becomes 1.1×10^7 S/m and the simulated S_{21} is reduced to between -1.2 dB and -0.8 dB. This also agrees very well with the measured S_{21} after second gold coating. The VDI waveguide showed better performance, with measured S_{21} between -0.6 dB and -0.4 dB, which almost matches the simulated result of an ideal gold coated waveguide. The insertion loss results at a nominal frequency of 180 GHz are given in Table III for comparison.

These results from both the filters and the waveguide sections show: (1) The loss of these waveguide components can be reasonably predicted when surface roughness is considered. (2) The relatively high surface roughness is an important limiting factor for 3D printed waveguide components and therefore effective post-processing technique is required in order to obtain a performance close to theoretical limits. To this end, polishing techniques, applicable to small, enclosed structures, such as abrasive flow machining (AFM) [35] or electrochemical polishing [36] may be utilized. The AFM may be applied to straight-through waveguide sections. However, for waveguide cavity filters, the method may not be a suitable polishing approach as the small coupling iris features may be distorted. In [36], electrochemical process has been applied to 3D printed metal tubes with various geometries and it was successful in reducing internal surface roughness S_a from more than 15 µm to less than 6 µm. However, the process needs to be further investigated and developed for small waveguide structures like the parts presented here.

The performance of the waveguide sections is compared with other reported 3D-printed sections at various frequency bands [4]-[10] in Table IV. The dissipative attenuation of each waveguide is given in [dB/m]. This attenuation is due to dissipated or ohmic losses associated with the internal surfaces of a waveguide with physical length l and is calculated as follows [37]:

$$\alpha_D = -\frac{10}{l} \times log_{10}\left(\frac{|S_{21}|^2}{1-|S_{11}|^2}\right) \quad [\text{dB/m}] \qquad (1)$$

The attenuation α_D of the MLS gold-plated monolithic waveguide is 15 dB/m at 180 GHz. It is lower than other reported 3D-printed WR-5 waveguides: 59 dB/m at 172 GHz in [5] and 90 dB/m at 220 GHz in [10]. The commercial high-precision waveguide section from VDI still shows superior performance with an attenuation of 7.7 dB/m at 180 GHz.

V. Conclusion

Monolithic waveguide filters operating at 180 GHz and a monolithic G-band waveguide section, all fabricated by MLS process, have been comprehensively evaluated. The RF measurements of the as-printed stainless steel devices showed high insertion losses, about 3 dB for the filters and a frequency dependent 4.7 dB to 7 dB for the waveguide section. This was due to the relatively low electrical conductivity of the stainless steel alloy (1.35×10^6 S/m) as well as the high surface roughness (Sa~3.65 μm). Successive application of electroless gold plating has significantly reduced the insertion losses, to about 0.5 dB in the filter samples and about 0.7 dB to 1 dB in the waveguide section. One of the filter samples was inspected utilizing micro-CT scan and then cut using EDM to further investigate the internal surfaces and dimensions. Measurements showed good build quality and average dimensional deviation from design values of about ±10 μm . Comparison between the two filter samples confirmed excellent repeatability of the MLS process and good consistency in the coating quality. Detailed comparison between simulation and measurements also shows that the insertion loss of the waveguide components can be predicted with good accuracy when surface roughness is considered. It also reveals the surface roughness is the main limiting factor for the 3D printed components. This points to a requirement for further development of post-processing surface polishing techniques suitable for small enclosed monolithic structures, such as electrochemical polishing. It should be noted that no polishing technique was applied to the internal surfaces of the presented components. The investigative study has demonstrated the capability and some of the constraints of 3D printing technology in fabrication of waveguide devices for sub-terahertz applications.

References

[1] S. S. Crump, “Modeling apparatus for three-dimensional objects,” U.S. Patent 5 340 433, Jun. 8, 1992.

[2] C. W. Hull, “Apparatus for production of three-dimensional objects by stereolithography,” U.S. Patent 4 575 330, Aug. 8, 1984.

[3] C. R. Deckard, “Method and apparatus for producing parts by selective sintering,” U.S. Patent 4 863 538, Oct. 17, 1986.

[4] M. D’Auria *et al*., "3-D Printed Metal-Pipe Rectangular Waveguides," in *IEEE Transactions on Components, Packaging and Manufacturing Technology*, vol. 5, no. 9, pp. 1339-1349, Sept. 2015.

[5] S. Lucyszyn, X. Shang, W. J. Otter, C. W. Myant, R. Cheng and N. M. Ridler, "Polymer-based 3D Printed Millimeter-wave Components for Spacecraft Payloads," *2018 IEEE MTT-S International Microwave Workshop Series on Advanced Materials and Processes for RF and THz Applications (IMWS-AMP)*, 2018, pp. 1-3.

[6] A. von Bieren, E. de Rijk, J. Ph. Ansermet and A. Macor, "Monolithic metal-coated plastic components for mm-wave applications," *2014 39th International Conference on Infrared, Millimeter, and Terahertz waves (IRMMW-THz)*, 2014, pp. 1-2.

[7] W. Otter et al., “3D printed 1.1 THz waveguides”, *IET Electronics Letters*, vol. 53, no. 7, pp. 471-473, Mar. 2017.

[8] B. Zhang and H. Zirath, "Metallic 3-D Printed Rectangular Waveguides for Millimeter-Wave Applications," *IEEE Transactions on Components, Packaging and Manufacturing Technology*, vol. 6, no. 5, pp. 796-804, May 2016.

[9] K.V. Caekenberghe, P. Bleys, T. Craeghs, M.J. Pelk and S.V. Bael, “A W-band waveguide fabricated using selective laser melting,” *Microwave and Optical Technology Letters*, vol. 54, no. 11, pp. 2572-2575, 2012.

[10] V. Fiorese *et al*., "Evaluation of Micro Laser Sintering Metal 3D-Printing Technology for the Development of Waveguide Passive Devices up to 325 GHz," *2020 IEEE/MTT-S International Microwave Symposium (IMS)*, 2020, pp. 1168-1171.

[11] B. Zhang *et al*., "Metallic 3-D Printed Antennas for Millimeter- and Submillimeter Wave Applications," *IEEE Transactions on Terahertz Science and Technology*, vol. 6, no. 4, pp. 592-600, July 2016.

[12] S. Shin, X. Shang, N. Ridler and S. Lucyszyn, “Polymer-based 3-D printed 140-220 GHz low-cost quasi-optical components and integrated subsystem assembly”, *IEEE Access*, vol. 9, pp. 28020-28038, Feb. 2021.

[13] S.-H. Shin, R. Payapulli, L. Zhu, M. Stanley, X. Shang, N. M. Ridler, and S. Lucyszyn, “3-D printed plug and play prototyping for low-cost sub-THz subsystems”, *IEEE Access*, vol. 10, pp. 41708-41719, Apr. 2022.

[14] C. Guo, X. Shang, M. J. Lancaster and J. Xu, "A 3-D Printed Lightweight X-Band Waveguide Filter Based on Spherical Resonators," *IEEE Microwave and Wireless Components Letters*, vol. 25, no. 7, pp. 442-444, July 2015.

[15] X. Shang *et al*., "W -Band Waveguide Filters Fabricated by Laser Micromachining and 3-D Printing," *IEEE Transactions on Microwave Theory and Techniques*, vol. 64, no. 8, pp. 2572-2580, Aug. 2016.

[16] L. Zhu, R. Payapulli, S.-H. Shin, S-H, M. Stanley, N. M. Ridler, S. Lucyszyn, “3-D printing quantization predistortion applied to sub-THz chained-function filters”, *IEEE Access*, vol. 10, pp. 38944-38963, Mar. 2022.

[17] O. A. Peverini et al., “Additive manufacturing of Ku/K-band waveguide filters: A comparative analysis among selective-laser melting and stereo-lithography,” *IET Microw., Antennas Propag.*, vol. 11, no. 14, pp. 1936–1942, Nov. 2017.

[18] P. Booth and E. V. Lluch, "Enhancing the Performance of Waveguide Filters Using Additive Manufacturing," *Proceedings of the IEEE*, vol. 105, no. 4, pp. 613-619, April 2017.

[19] P. Booth, "Additive Manufactured Bandpass Filters at Ka-band," *IEEE MTT-S International Microwave Workshop Series on Advanced Materials and Processes for RF and THz Applications (IMWS-AMP)*, 2019, pp. 7-9.

[20] B. Zhang and H. Zirath, "A Metallic 3-D Printed E-Band Radio Front End," *IEEE Microwave and Wireless Components Letters*, vol. 26, no. 5, pp. 331-333, May 2016.

[21] M. Salek et al., "W-Band Waveguide Bandpass Filters Fabricated by Micro Laser Sintering," *IEEE Transactions on Circuits and Systems II: Express Briefs*, vol. 66, no. 1, pp. 61-65, Jan. 2019.

[22] T. Skaik, M. Salek, Y. Wang, M. Lancaster, T. Starke and F. Boettcher, "180 GHz Waveguide Bandpass Filter Fabricated by 3D Printing Technology," *13th UK-Europe-China Workshop on Millimetre-Waves and Terahertz Technologies (UCMMT)*, 2020, pp. 1-3.

[23] T. Skaik *et al*., "A 3-D Printed 300 GHz Waveguide Cavity Filter by Micro Laser Sintering," in *IEEE Transactions on Terahertz Science and Technology*, vol. 12, no. 3, pp. 274-281, May 2022.

[24] J. Ding, S. Shi, K. Zhou, D. Liu and W. Wu, "Analysis of 220-GHz Low-Loss Quasi-Elliptic Waveguide Bandpass Filter," *IEEE Microwave and Wireless Components Letters*, vol. 27, no. 7, pp. 648-650, July 2017.

[25] X. H. Zhao *et al*., "D-Band Micromachined Silicon Rectangular Waveguide Filter," in *IEEE Microwave and Wireless Components Letters*, vol. 22, no. 5, pp. 230-232, May 2012.

[26] X. H. Zhao et al., "G-band rectangular waveguide filter fabricated using deep reactive ion etching and bonding processes", *IET Micro Nano Lett.*, vol. 7, no. 12, pp. 1237-1240, Dec. 2012.

[27] D. Stephens, P. R. Young and I. D. Robertson, "Design and Characterization of 180 GHz Filters in Photoimageable Thick-Film

Technology," *IEEE MTT-S International Microwave Symposium Digest, 2005.*, 2005, pp. 451-454.

[28] X. Chen, J. Hu and X. Le, "G-Band Diplexer Based on E-Plane Waveguide Structures," *2018 Progress in Electromagnetics Research Symposium (PIERS-Toyama)*, 2018, pp. 1343-1346.

[29] Computer Simulation Technology (CST) Microwave Studio Suite 2019, Accessed: Feb. 1, 2022. [Online]. Available: http://www.cst.com

[30] Jia-Sheng Hong and M.J. Lancaster, "Microstrip filters for RF/ Microwave applications", John Wiley and Sons Inc, 2001.

[31] 3D Micro Print GmbH. Accessed: Feb. 1, 2023. [Online]. Available: http://www.3dmicroprint.com/

[32] Alicona InfiniteFocus, Accessed: Feb. 1, 2023. [Online]. Available: http: //www.alicona.com/products/infinitefocus/

[33] K. A. Ibrahim, B. Wu, N. P. Brandon, "Electrical conductivity and porosity in stainless steel 316L scaffolds for electrochemical devices fabricated using selective laser sintering", *Materials and Design*, vol. 106, pp. 51-59, 2016.

[34] E. Hammerstad and O. Jensen, "Accurate models for microstrip computer-aided design," in *IEEE MTT-S Int. Microw. Symp. Dig.*, Washington, DC, May 1980, pp. 407–409.

[35] C. Bouland, V. Urlea, K. Beaubier, M. Samoilenko and V. Brailovski, "Abrasive flow machining of laser powder bed-fused parts: Numerical modeling and experimental validation," *Journal of Materials Processing Technology*, vol. 273, 2019.

[36] U. Ali, H. Fayazfar, F. Ahmed, and E. Toyserkani, "Internal surface roughness enhancement of parts made by laser powder-bed fusion additive manufacturing," *Vacuum*, vol. 177, Jul. 2020.

[37] B. Zhang, Y. -X. Guo, H. Zirath and Y. P. Zhang, "Investigation on 3-D-Printing Technologies for Millimeter- Wave and Terahertz Applications," in *Proceedings of the IEEE*, vol. 105, no. 4, pp. 723-736, April 2017.

Talal Skaik received M.Sc. degree in communications engineering and P.hD. degree in microwave engineering from the University of Birmingham, Birmingham, U.K., in 2007 and 2011, respectively.

After PhD, he worked in lecturing in electrical engineering until 2019. He is currently working as a research fellow in the Electronic, Electrical and Systems Engineering Department at the University of Birmingham. He has authored/co-authored over 30 refereed research papers. He acts as a reviewer for various microwave journals and for the European Microwave Conference (EuMC). His research interests include millimeter-wave and terahertz filters and antennas, 3D-printed microwave devices, temperature compensated filters for satellite payloads, multi-port coupled resonator structures and energy harvesting circuits.

Milan Salek received the BEng degree in Electrical and Electronic Engineering from the Aston University, Birmingham, U.K., in 2016, and the Ph.D. degree in Microwave Engineering from the University of Birmingham, Birmingham, U.K., in 2019. Presently he is a Research Fellow in the Department of Electronic, Electrical and Systems Engineering, University of Birmingham. His current research interests include 3-D printed passive microwave devices, bolometric and diode-based power sensors, as well as millimeter-wave and terahertz circuits.

Peter Hunyor holds a BEng (Hons) and a diploma in natural sciences. He is certified Airline and Aerospace surface finisher by NASF (National Association for Surface Finishing, USA). He joined the Science and Technology Facilities Council (STFC) as a process engineer in 2015 and has been working on various surface finishing and inspection techniques ever since. He is managing the gold-plating & electro-forming laboratory and the materials analysis laboratory within the MMT Group. He is currently working on the European Space Agency (ESA's) MetOp project where he successfully validated multiple surface finishing processes for flight. His current research interests include additive manufacturing and high precision electroforming to develop corrugated feedhorns.

Hui Wang received her M.Sc. and Ph.D. degree in astrophysics and space instrumentation from University Pierre and Marie Curie, Paris, France in 2005 and 2009 respectively. She joined RAL Space in 2009 as a Millimetre Wave Design Scientist/Engineer and works as a key member of the Millimetre Wave Technology Group. She is currently leading Schottky diode device development within the Group. Her general interests include millimetre wave and THz devices, primarily heterodyne frequency mixers and harmonic up-conversion multipliers, in support of Earth observation and astronomy remote sounding experiments.

Peter Huggard graduated from Trinity College Dublin, Republic of Ireland, in 1987 with a degree in Experimental Physics. This was followed by a PhD on the generation and detection of short pulsed terahertz radiation. After post-doctoral research at universities in Regensburg, Germany, and Bath, UK, and lecturing in physics at Bath, he joined the CCLRC Rutherford Appleton Laboratory in 2000. He is now Research Council's Individual Merit Band G, and leader of the Millimetre Wave Technology Group. He also leads new terahertz technology development within the Group, working on detectors, sources, filters, instruments and instrument calibration technology. Applications of his work include active and passive remote sensing of the Earth's atmosphere, and radio astronomy.

Dr. Huggard is a chartered physicist and also senior member of the IEEE and the OSA. He has authored over 60 refereed publications and acts as a referee for several international physics and engineering journals. He also holds a visiting

professorship at the Department of Electrical and Electronic Engineering, University College London.

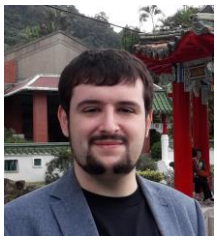

Paul Wilson received an MSc degree in Palaeobiology from the University of Bristol, U.K., in 2014 before completing a PhD in Engineering from the University of Warwick, U.K., in 2019.

He currently works at the University of Warwick as a Research Fellow, following directly on from their PhD project in applying X-Ray CT to inter-disciplinary use-cases through the National X-Ray Computed Tomography facility (NXCT). His main research interests include palaeobiology and the application of digital technologies in cultural heritage.

Mark A Williams received an MSc degree in Advanced Manufacturing Technology from the University of Manchester Institute of Science and Technology, U.K., in 1995 before completing a PhD in Mechanical Engineering from the same institution in 1998.

He currently works as a Professor at WMG, the University of Warwick heading the Centre of Imaging, Metrology, and Additive Technologies (CiMAT). His main research interests include the application of X-Ray Computed Tomography (XCT) and additive manufacturing in forensic applications, cultural heritage, metrology, and manufacturing.

Prof. Williams currently manages the University of Warwick branch of the National X-Ray Computed Tomography facility (NXCT), providing access to XCT facilities for interdisciplinary applications across the UK and overseas.

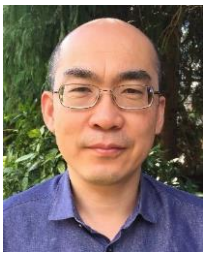

Yi Wang (M'09–SM'12) was born in Shandong, China. He received the B.Sc. degree in applied physics and M.Sc. degree in condensed matter physics from the University of Science and Technology, Beijing, China, in 1998 and 2001, respectively, and the Ph.D. degree in electronic and electrical engineering from the University of Birmingham, Edgbaston, Birmingham, U.K., in 2005.

From 2004 to 2011, he was a Research Fellow at the University of Birmingham. In 2011, he became a Senior Lecturer and then Reader at the University of Greenwich, U.K.. He is currently Associate Professor with the University of Birmingham. He is the author of over 170 research papers and has been the reviewer of several major microwave, antenna and sensor journals and an Associate Editor of IET MAP. He serves the TPC Chair of 2021 European Microwave Conference. His current research interests include multiport filtering networks, filter-antenna integration, millimeter-wave and terahertz antennas and devices for metrology, communication, and sensing. He is particularly interested in working with new materials and novel manufacturing techniques, such as micromachining and 3D printing, for RF/microwave applications.